Synchrotron Imaging of Li Metal Anodes in Solid State Batteries Aided by Machine Learning

Marm B. Dixit,[†] Ankit Verma,[‡] Wahid Zaman,[†] Xinlin Zhong,[†] Peter Kenesei,[¶] Jun Sang Park,[¶] Jonathan Almer,[¶] Partha Mukherjee,[‡] and Kelsey B. Hatzell[*,†,§,‖]

†*Department of Mechanical Engineering, Vanderbilt University, Nashville, TN, USA, 37240*

‡*School of Mechanical Engineering, Purdue University, West Lafayette, IN, USA, 47907*

¶*X-Ray Science Division, Advanced Photon Source, Argonne National Laboratory, Lemont, IL, USA, 60439*

§*Chemical and Biomolecular Engineering, Vanderbilt University, Nashville, TN, USA,37240*

‖*Interdisciplinary Material Science Program, Vanderbilt University, Nashville, TN, USA, 37240*

E-mail: *kelsey.b.hatzell@vanderbilt.edu

Phone: +1 (615)-875-8391

Abstract

Reversible lithium metal anodes that can achieve high rate capabilities are necessary for next generation energy storage systems. Solid electrolyte can act as a barrier for unwanted physical and chemical decomposition that lead to unstable electrodeposition (e.g. dendrite and filament growth). The formation and growth of filaments is tied to unique chemo-mechanical properties that exists at buried solid|solid interfaces. Herein, *in situ* tomography of Li|LLZO|Li cells is carried out to track morphological transformations in Li metal electrodes and buried solid|solid interfaces during stripping and plating processes. Optimized experimental parameters provide high resolution, high contrast reconstructions that enable lithium metal visualization. Machine learning and image processing tools are combined to quantify changes in lithium metal during stripping and plating. The analysis enables quantifying local current densities and pore size distribution in lithium metal during cycling experiments. Hotspots in lithium metal are correlated with microstructural anisotropy in the solid electrolyte. Modeling studies show large heterogeneity in transport and mechanical properties of electrolyte at the electrode|electrolyte interfaces. Regions with lower effective properties (transport and mechanical) are nuclei for failure. Failure is attributed to microstructural heterogeneities in the solid electrolyte that lead to high local stress and flux distributions.

Lithium metal anodes can enable energy dense solid state batteries.[1] However, lithium metal can form filaments that grow into a solid electrolyte (SE) and cause failure via fracture or electrical shorting. These failure mechanisms limit the power density and Coulombic efficiencies of all-solid-state batteries.[2] Monroe and Newman suggested a high shear modulus solid electrolyte (more than two times the lithium shear strength) could eliminate electrodeposition instability mitigating dendrite formation.[3] However, this theoretical guideline has not been observed in experimental studies for a wide range of solid electrolytes.[4–9] Furthermore, both soft (sulfide) and hard (oxide) solid electrolytes can experience shorting at low current densities. This limits high rate and reversible cycling of lithium metal in solid state batteries. Pores can form in lithium metal at the solid electrolyte interface at high stripping rates (e.g. current density). Pores/voids can form because of mass transport imbalances at this interface[5,10] (Fig. 1A). Typically, these pores form at defects and/or microstructure heterogeneities and may be a nucleation site for filament formation and growth.[5] Furthermore, voids/pores can lead to electrode delamination and local regions with high current densities and stress concentration.[11] High local over-potentials in these regions can lead to nucleation and preferential growth of lithium through these sites.[12,13] While a phenomenological understanding of the filament onset and growth mechanism exists, there are only limited experimental investigations that provide direct *in situ* observations of the origin of electrodeposition instabilities at solid electrolyte interfaces.[6,14]

Lithium filament formation and growth in polycrystalline inorganic solid electrolytes is complex. Microstructural heterogeneities (e.g. grain,defects[11,15,16]), lithium metal mechanics,[17] and operating current densities[4,18,19] can all impact the morphology, growth pathway, and severity of the shorting event. Li^+ molar volume mismatch between lithium metal, solid electrolyte interfaces, and confined regions (grain boundaries, defects, stressed interfaces) make localized deposition favorable compared to planar deposition.[13] Furthermore, fensity functional theory (DFT) studies suggest that lithium plating prefers regions with lower elastic modulus (e.g. grain boundaries).[20] Finally, interface and surface roughness has also been identified as a crucial factor dictating filament nucleation and growth.[21] Recently, a few experimental studies have suggested that lithium filament growth is affected by stack pressure.[10,14,17] The latter result suggests that non-uniform contact upon electrochemical cycling may be a significant driver for filament growth. However, the intricate interdependencies between microstructure (grain boundaries, defects), operating conditions (e.g. pressure), and interface kinetics and transport (Li^+ molar volume mismatch) is complex and not well understood with respect to lithium filament growth in solid electrolytes.

High-resolution imaging of lithium metal at buried solid|solid interfaces is challenging because low atomic number elements weakly interact with experimental probes (neutrons, electrons, X-rays). Additionally, for *in situ* and *operando* imaging, proximity to highly absorbing/scattering materials (steel current collector, $Li_7La_3Zr_2O_12$ -LLZO electrolyte) significantly impedes extracting morphological information from lithium metal. Maintaining a stable, air-free environment during operation is also a key experimental challenge. Filament formation is typically characterized by *ex situ* optical/electron microscopy due to these experimental challenges.[19,22,23] Recent *operando* optical imaging of Li|LLZO|Li systems demonstrated how the morphology of the filament different depending on the operating regime (e.g. current density) which suggests that there are a variety of failure mechanisms.[9] Transmission electron microscopy imaging has revealed nanometer level tetragonal LLZO interphase formation at the Li|cubic-LLZO interface.[24] Interphase formation can also induce mechanical stresses due to volume expansion leading to chemo-mechanical failure.[1] While microscopy and optical imaging offer valuable material insight, it is difficult to extrapolate the information gleaned at the nm-level to macroscopic interfaces in actual batteries reliably. Synchrotron X-ray tomography is a potential method to resolve three-dimensional morphological transformations with adequate spatial and temporal resolutions relevant to solid state batteries.[25–29]

Currently, it is very challenging to discern lithium electrode kinetics at solid electrolyte interfaces. This work uses imaging techniques to track morphological transformations at lithium metal/solid electrolyte interfaces. A garnet (LLZO) solid electrolyte is chosen as the model electrolyte to image because it is one of the most stable solid electrolytes, and has minimal interphase formation. The formation of an interphase, makes it challenging to directly probe lithium metal electrode kinetics. Herein, lithium metal imaging is achieved via leveraging principles of phase- and absorption- contrast. *In situ* studies of the Li|LLZO|Li system enable direct observation of morphological transformations in lithium metal during plating/stripping. In order to process the low-contrast images (lithium metal and pores) advanced image processing and machine learning methods were developed for effective segmentation to extract quantitative metrics of the electrodes (current density, porosity and their spatial distribution) during cycling. Spatial variation in microstructrural properties of the solid electrolyte are correlated to the hotspot generation within the lithium metal (Fig. 1a). Mesoscale simulations of the solid electrolyte reveal heterogeneous transport and mechanical properties. Failure onset at Li|SE interfaces occurs at regions with lower transport and mechanical properties.

X-ray imaging relies on absorption and phase contrast to distinguish materials in the field of view of the beam. Absorption contrast captures differences in the attenuation of the

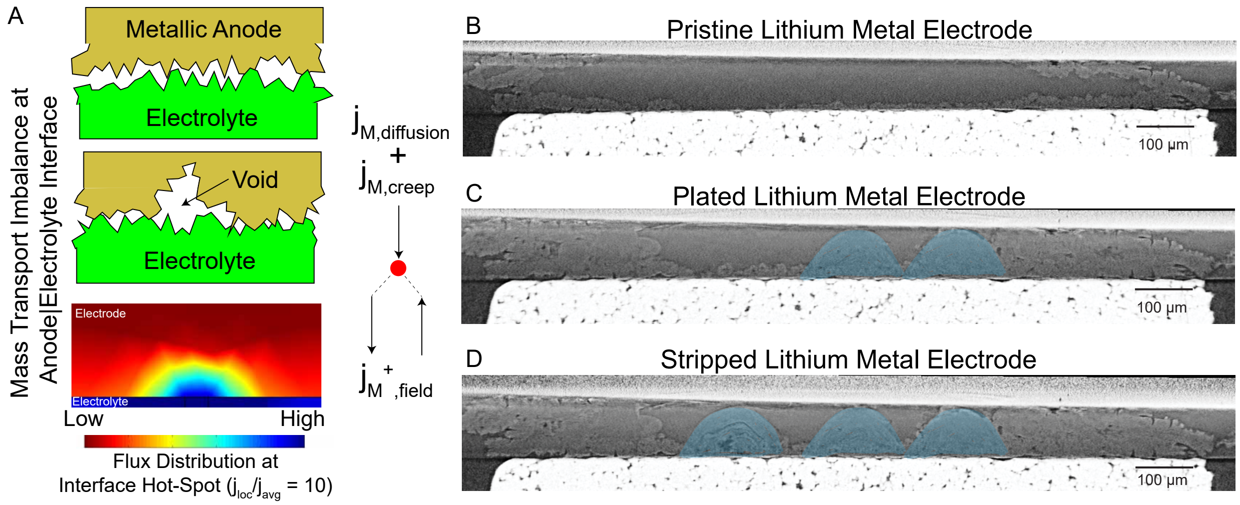

Figure 1: (a) Schematic diagram of the interfacial transport challenges in lithium metal solid-state batteries.$j_{M,diffusion}$ and $j_{M,creep}$ represents vacancy diffusion in lithium metal and transport occurring due to plastic deformations during creep. $j_{M^+,field}$ is the ion flux to the interface from within the solid electrolyte. Flux imbalance at the interface can lead to generation of voids/non-planar deposition events. Computation fluid dynamics simulations are carried out over an ideal domain with an interfacial region exhibiting a high local current density (j_{loc}/j_{avg}=10). Lithium ion flux distribution profiles around the hotspot into the electrode are visualized. (b-d) Sample reconstruction slices of lithium metal electrode imaged for pristine, plating and stripping steps. Semi-circular morphologies matching the flux profiles are observed in the plating as well as stripping electrode and are highlighted for better visualization.

X-rays along the trajectory from the source to the detector. The attenuation depends on the spatial density of the material, depth of the sample and the incident X-ray wavelength. Assuming there is one material in the X-ray beam, this attenuation is described by the Beer-Lambert law:

$$I(x,y,\lambda) = I_0(x,y)exp\big[-(\mu_0^\lambda - \mu_h^\lambda)T_0(x,y)\big] \tag{1}$$

where I is the attenuated intensity, I_0 is the incident intensity, μ_0^λ is the attenuation coefficient of air, μ_h^λ is the attenuation coefficient of sample for X-rays of wavelength λ, and T_0 is the projected thickness through point (x,y) in the direction of z, which is the propagation direction of the X-ray beam. In addition to attenuation, X-rays will undergo a phase shift after traversing a material. The phase shift is determined by the real part of the complex refractive index of the material which depends on the incident X-ray wavelength and local electron density. The phase shift imparted by the sample to the X-ray is given by,[30]

$$\Phi(x, y, \lambda) = -k \int_O dz \delta(x, y, z, \lambda) \tag{2}$$

where Φ is the phase shift, δ is the real part of the complex refractive index (in terms of n=1-δ+iβ), k is a proportionality constant and the integration is carried out over the extent of object O along the optical axis. While it is not possible to directly measure the phase of the transmitted X-rays, the interference pattern is captured and reconstructed. The phase contrast is enhanced specifically at the interfaces between materials. Distinguishing low density phases (pores, lithium metal) is challenging for larger sample sizes as well as without adequate phase contrast. The careful combination of absorption and phase contrast and experimental design enables lithium metal imaging at buried solid|solid interfaces. Monochromatic, high energy X-rays (E = 76.2 keV) are employed for imaging the Li|LLZO|Li system. High monochromaticity ($\Delta E/E \approx 10^{-3}$) allows to distinguish low contrast differences. The transverse sample thickness was reduced to about 1.5 mm to match the field-of-view. Sample-detector distance was selected to ensure optimum phase contrast. GRIDREC reconstruction algorithm was used to ensure high quality reconstructions.[31] Critical current density of approximately 26 μA cm^{-2} was identified from the *in situ* experiments (Fig. S1). Limitation in assembling a 1.5 mm diameter cell and absence of stack pressure results in a relatively lower critical current density compared to those typically reported for LLZO.[6] The low initial polarization ($\approx$ 20-40 mV) and cell impedance values ($\approx$ 2000 Ω cm^{-2}) are comparable to previous *ex situ* measurements[4] which suggest that the transformations identified here are probing the material limitations. The sample size was dictated by the field-of-view available and to restrict signal interference for obtaining high-contrast images. Larger samples (bigger than 3 mm) can achieve high critical current densities and are easier to assemble. However, these samples cannot achieve critical contrast information due to scattering/absorption from outside the field-of-view. For this study, we sacrifice critical current density (large samples) because our intention is to resolve transformations in the lithium metal at dense LLZO interfaces, which requires small field of view (and samples). Reconstruction across different electrochemical steps show marked differences in lithium metal electrode (Fig. 1b-d, S2-3). Optimized experimental and reconstruction protocols enable visualizing of morphology variation in lithium metal as well as presence of pores within the electrode. Semicircular domains (highlighted in planar sections, Fig. 1c,d) are visualized in lithium metal on plating as well as stripping. This morphology closely resembles lithium ion flux profiles around a hotspot at the electrode|electrolyte interface. Such deposition morphologies were postulated in earlier work.[10] This is the first mesoscale experimental observation of such morphologies in lithium metal electrodes at solid electrolyte interfaces. Stripping from the same electrode leads to formation of a similar semicircular feature with the presence of voids (darker regions) near the interface (Fig. 1d). Regions in the center of a stripping hotspot would have higher mass flux leaving the domain leading to generation of voids due to flux imbalance (Fig. 1a).

In situ tomography data set can generally be large in size particularly if the sample is large and many electrochemical steps are probed. A typical tomography scan of a symmetric cell results in a data-set greater than 30 GB. Tracking pixel level changes in morphology of lithium metal across these datasets is prohibitive. An analytical approach was developed to enable faster analysis via finding regions of interest (Fig. 2a). Regions of interest are considered location where either pores form in lithium metal, delamination may occur, and/or nucleation sites for filament formation. To identify these regions of interest we quantified a spatial current density profile across the lithium metal. This can be estimated by tracking the thickness of the electrode over different electrochemical steps given as,

$$j_{i,j} = \frac{(t_{2,i,j} - t_{1,i,j}) * F}{\Delta t * V_{Li}} \tag{3}$$

where $j_{i,j}$ is the spatial current density at location specified by coordinates i and j, $t_{2,i,j}$

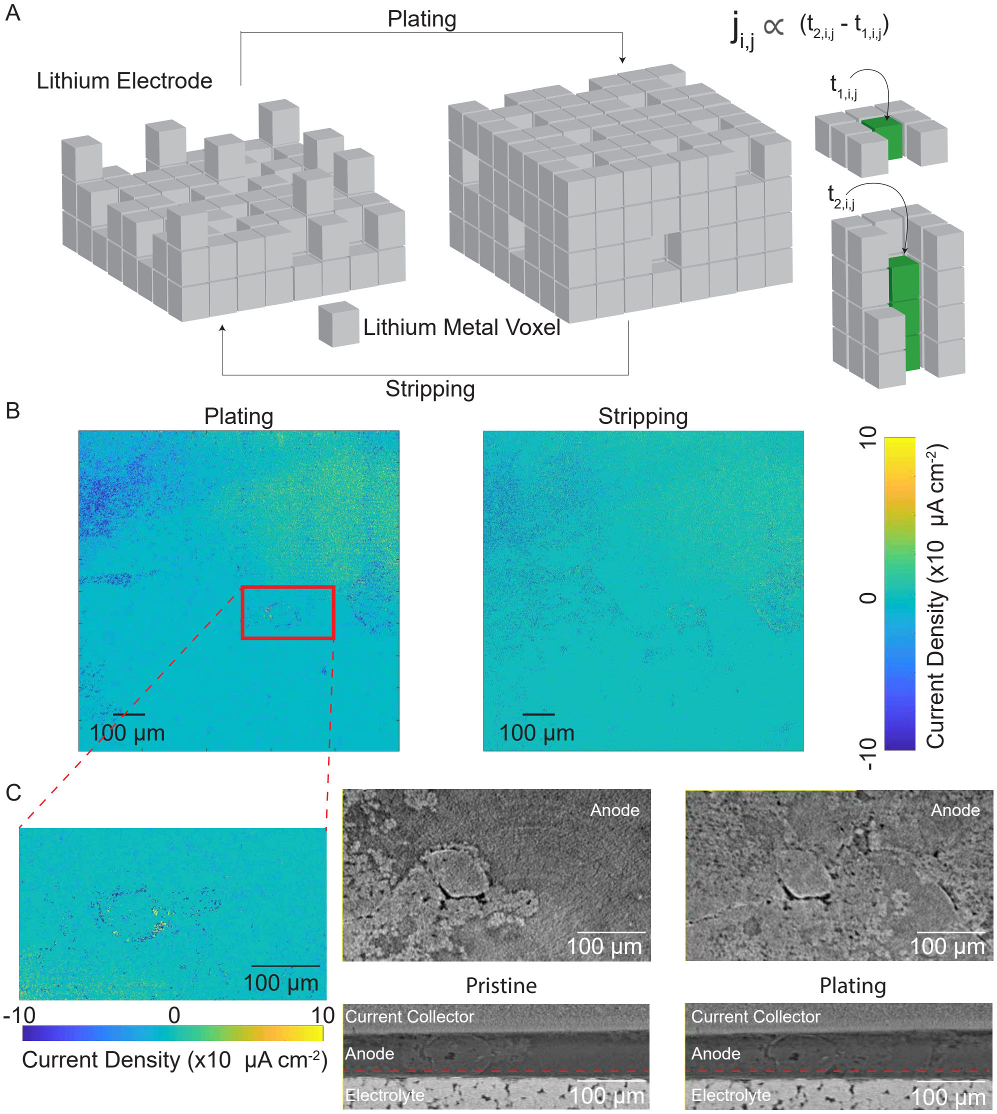

Figure 2: (a) Schematic diagram describing the current density quantification method. Difference in lithium electrode thickness are evaluated at each location across the electrode area. The local current density is proportional to the difference of the thickness of lithium electrode in successive image sets. (b) Current density maps for plating and stripping steps of a single electrode. (c) Expanded region identified as possessing potential hotspots region and the corresponding sectional images from the raw tomography data. Regions with uniform current density shows evidence of planar deposition, while the locations with lower current density directly correlate to the presence of pores/voids within the electrode. Additionally, differences in the sub-surface electrolyte microstructre in these sections are clearly visible.

and $t_{1,i,j}$ are thickness of lithium metal electrode at steps 1 and 2, F is Faraday's constant, Δt is the time duration of electrochemical cycle and V_{Li} is the molar volume of lithium. The thickness of lithium metal electrode was estimated by measuring intensity line-profiles at each location through the depth of the sample. Distinct absorption contrast between steel (current collector) and LLZO electrolyte enables identification of the electrode thickness. This measurement can be easily automated enabling faster tracking of the data-sets by providing qualitative information for easier identification of hotspots. Specifically, with the current data-set mapping current density over a 1 mm^2 area for both electrodes in a symmetric cell takes ≈20 min. Spatial current density maps for plating and stripping cycle show significant variation (Fig. 2b). Most of the lithium metal shows a uniform current density and is denoted by green/blue (Fig. 2b,c). There are isolated spots that demonstrate either a greater than average current density (yellow) or lower than average current density (blue). A potential hotspot region (yellow) is identified from the current density plots for further analysis of the raw projections (Fig. 2c). Comparing pristine and plating morphologies of the identified section shows the presence of interfacial pores as well as globular depositions. In addition to different plating morphologies, a clear difference in the electrolyte microstructure is observed for the hotspot region identified. Analysis of additional hotspot regions across multiple cycles show consistent results (Fig. S4-5). Spatial current density mapping aids in identifying local hot spots. Combining spatial current density mapping with imaging allows for directly tracking meso- and microstuctural properties that may impact the formation of hotspots while reducing the analysis time and computational power required for assessment of *in situ* tomography data.

Quantification of microstructural properties (pores/voids) in the lithium electrode is possible due to the high contrast imaging, but requires a rigorous segmentation procedure. Conventional thresholding methods cannot segment the phases (pores vs. lithium) reliably and manual segmentation of the entire data-set is prohibitive. Convolutional neural networks is a machine learning method widely used for semantic segmentation in a wide range of disciplines

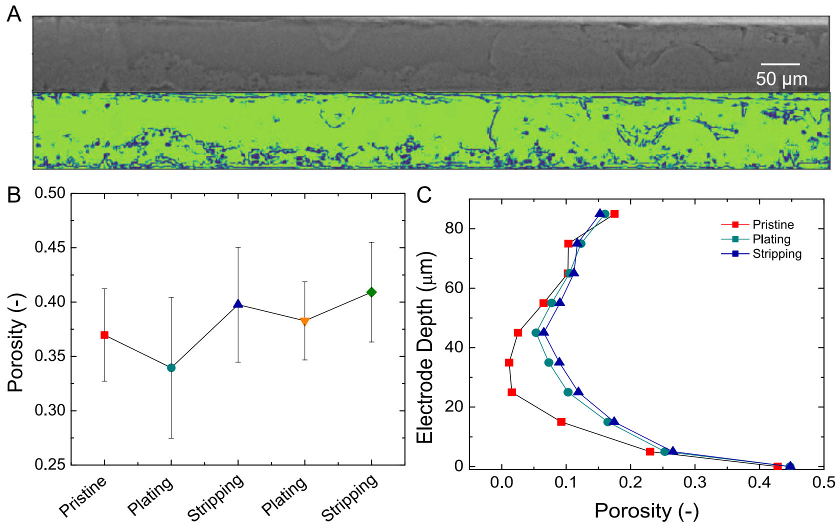

Figure 3: (a) Sample lithium electrode fed to the developed convolutional neural network and the resultant segmented data set obtained (b) Porosity variation of a single electrode at subsequent electrochemical cycling stages. This porosity is estimated near the solid electrolyte interface.(c) Porosity distribution as a function of electrode depth at various electrochemical cycling stages. The quantification metrics are evaluated from the segmented lithium electrodes obtained from the convolutional neural network. Identical pre-processing, segmentation and post-processing steps are employed for all the individual data-sets to enable comparison.

that enable pixel-level classification of large data-sets.[32–36] We implemented a resnet34 based deep convolution neural network for enabling lithium metal segmentation.[37] The neural network processed individual cross-sectional images of lithium metal to yield a high confidence segmented image (Fig. 3a). Individual slice segmentation times were approximately 0.3 s, with greater than 80% confidence in segmentation (Fig. S6). The segmentation times are an order of magnitude smaller than those typically needed for manual labelling of these images. These confidence statistics are competitive with the segmentation confidence obtained by state-of-the-art networks on standard data-sets. The neural network was trained on 800 images from one electrode in a single electrochemical cycle and validated on a further 200 additional images from the same electrode. Training and validation data was generated by computationally edge-segmented and manually corrected images. The quantification metrics discussed are obtained from the segmented images obtained by applying the trained network to all the subsequent data-sets. It should be noted that the segmentation introduces some error in quantification (80% confidence). Absolute quantification is not advised; however, relative trends between successive electrochemical steps can be ascertained. Pre-processing, segmentation, and post-processing steps are identical for all the evaluated data-sets enabling comparative evaluation.

Pristine lithium metal has a porosity of around 10%. Mass transport imbalance at the Li |SE interface is widely postulated to generate voids at the interface in solid-state batteries.[5,10] So far, limited cross-sectional imaging evidence is provided for this mechanism.[5] *In situ* tomography with high contrast for lithium metal enables quantitative assessment of this phenomena. Higher mass flux at the interface due to local high current density, poor lithium diffusion and creep can lead to pore formation. Inadequate metal diffusion and creep flow leads to generation of these voids. Porosity measured near the interface clearly reflects this phenomenological model proposed, with plating showing a reduction in porosity and stripping leading to an increase in porosity in the lithium metal (Fig. 3b). This behavior is also reflected over the entire electrode section as well with porosity increases from the plating step to the stripping step (Fig. S7). Pristine lithium metal demonstrates a single modal porosity probability distribution while the plated and stripped samples have a non-uniform (tri-modal) distribution. The tri-modal distribution indicate larger spatial variation (variance) within the electrode section introduced due to electrochemical cycling. Additionally, the pore distribution along the electrode depth can be visualized using the segmented data (Fig. 3c). Individual data points in this graph are obtained by averaging the porosity over 10 μm thickness. The porosity at the Li|SE is greater than in the bulk metal regions. The high porosity at the interface suggests the formation of voids and interfacial delamination. Electrochemical cycling induced changes in the porosity depth profile are identified closer to the solid electrolyte interface. Porosity values at the current collector are consistent across the electrochemical steps suggesting that this region does not undergo active morphological changes during cycling. These results match well with the anticipated flux profiles in the vicinity of interfacial hotspots (Fig. 1a) where in flux gradients are concentrated near the solid electrolyte interface with less impact of the hotspot near the current collector end. Such behavior is only expected in systems with thick lithium foil electrode (higher excess lithium). Moving to systems with limited or no excess lithium, morphological changes are expected to propagate through the entire bulk of lithium metal.

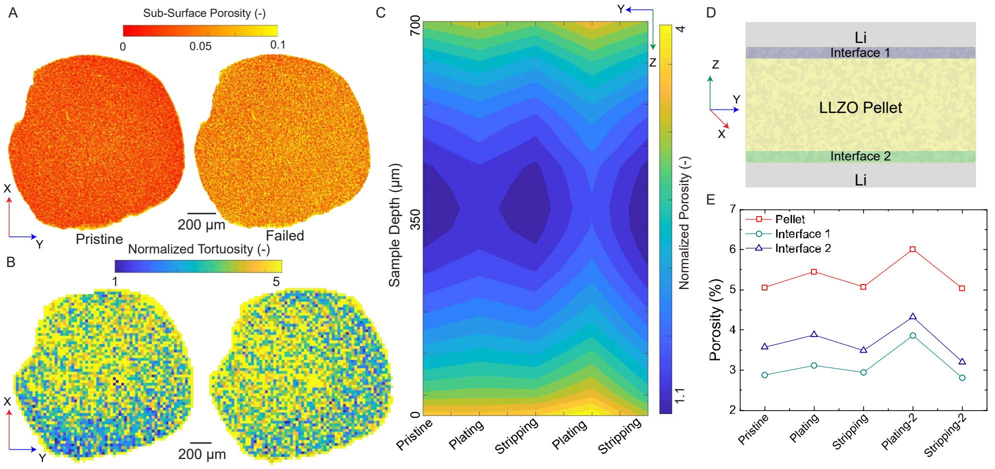

Figure 4: (a) Sub-surface porosity map measured through the depth of the sample for the pristine and the failed electrolyte pellet. (b) Spatial tortuosity factor distribution for pristine and failed sample. Tortuosity factors are estimated by carrying out simulations over 25x25x100 μm interfacial regions across the entire cross-section of the pellet. Steady state simulations under a constant concentration gradient are performed. (c) Spatial microstructural variation within the sample evaluated across multiple electrochemical cycling steps. Normalized porosity is plotted which is defined as the ratio of the local porosity to the average electrolyte porosity. Spatial resolution of 36 μm was used to assess the microstructural variation through the depth of the electrolyte. (d) Schematic diagram indicating physical location of the interfacial regions considered for simulations and analysis. (e) Bulk pellet porosity and interfacial porosity evaluated across each cycling step. Interfacial regions of 100 μm are considered for this analysis to correlate with the results obtained from the tortuosity factor calculations..

Microstructural changes occur in the lithium metal and the solid electrolyte during electrochemical cycling. Sub-surface porosity maps reflect the porosity averaged through the Z direction (sample depth) at each pixel along the lateral (XY) section. The solid electrolyte shows a systematic increase in the sub-surface porosity due to filament propagation (Fig. 4a, S8).[4] Using direct numerical simulations, tortuosity factors can be extracted in the bulk and interfacial region of the solid electrolyte. Tortuosity factors are determined along the Z direction which coincides with the electric field direction in the cell. Normalized tortuosity shown here is the relative change in local tortuosity factor compared to a completely solid domain (tortuosity factor = 1). This metric reflects the degree of obstruction the ions experience when transversing through the solid electrolytes. Piecewise simulations can capture microstructural heterogeneity over a large simulation domain which is not easily accessible via other modeling techniques (viz. computational fluid dynamics). Pristine and the failed samples show a distinct distribution of tortuosity factors within the interfacial region, with the failed sample showcasing a higher concentration of high tortuosity. High tortuosity regions lead to an effectively lower effective lithium ion flux through the domain as given by,[38]

$$J_{eff} = -D_{bulk}\,\frac{\epsilon}{\tau^2}\frac{\Delta c}{\Delta x} \tag{4}$$

where, D_{bulk} is effective diffusion coeffient in the bulk, ϵ is the porosity, τ is the tortuosity, $\frac{\Delta c}{\Delta x}$ is the effective concentration gradient. Regions of lower tortuosity surrounded by high tortuosity domains correspond to hotspots as lithium ion flux through the low tortuosity domains will be higher to ensure mass balance through the cell section. Variations in tortuosity factors across pristine and failed samples indicate a strong heterogeneity in the underlying microstructure. This effect is also apparent at individual plating and stripping steps (Fig. 4d-e, S9). The location and size of the x-ray transparent region (porosity) across the pellet as well as in the interfacial regions show a cyclic behavior with electrochemical steps. Average porosity clearly reflects a difference in the microstructure between successive electrochemical steps in the interfacial regions which is effectively captured in the simulations. It is known that single ion conductors theoretically do not show concentration gradients due to the unity transference numbers. However, the presence of pores has been identified to influence transport and failure mechanisms strongly.[4,39] The sub-surface porosity maps clearly highlight the spatial microstructural variation, specifically at the interfacial regions. Tortuosity factor maps provide evidence for transport heterogeneity due to the underlying microstructure variations. Hotspot generation leading to void and filament formation within the lithium metal electrode is linked with the microstructural heterogeneity identified in the solid electrolyte.

The average porosity of the pristine pellet was ≈5% indicating well-sintered, dense pellets. Normalized porosity shows a cyclic behavior with electrochemical cycles which decreases on plating and increases on stripping. The nominally X-ray transparent region (generically porosity) includes pores, voids as well as lithium deposition as these materials are difficult to distinguish within the bulk electrolyte. Modulation within this region can be interpreted as presence of electrochemically active lithium metal within the bulk electrolyte. The normalized pore density depth profile also shows spatial variation within the electrolyte domain with interfaces being more porous compared to the bulk. Higher amounts of X-ray transparent region at the interfaces can arise from crack/void generation from the mechanical stresses at the interface as well as from filament generation. Note that the spatial resolution used for laterally integrated porosity depth mapping is 36 μm which is higher than that was used for the simulation domains earlier. Averaging over a greater depth leads to lower porosity values for the interface (Fig. 4e, S8e) compared to that visualized here (Fig. 4c, S8c). Strong dependence of domain size on quantitative metrics further affirms the claim of microstructural heterogeneity within these dense pellets. Increasing the current density from 6 to 25 μA cm^{-2} on second plating/stripping cycles leads to greater penetration of the higher porosity regions into the bulk. This can reflect potential filament/crack propagation within the bulk. The spatial distribution is practically symmetric across the electrolyte depth suggesting identical mechanisms at both the plating and stripping electrodes. While the lithium metal electrode undergoes distinct morphological changes (void formation on stripping, non-planar deposition on plating), nominally identical response of LLZO electrolyte interfaces suggest they are influenced by the same underlying mechanics. Ion insertion and removal from the LLZO matrix at the interfaces causes stress generation within the solid electrolyte material. These phenomena lead to microstructural variations as evidenced by the tomography results. Further work on evaluating spatially resolved, grain-level chemo-mechanical response is required to understand the identical mechanical behavior at plating and stripping interfaces.

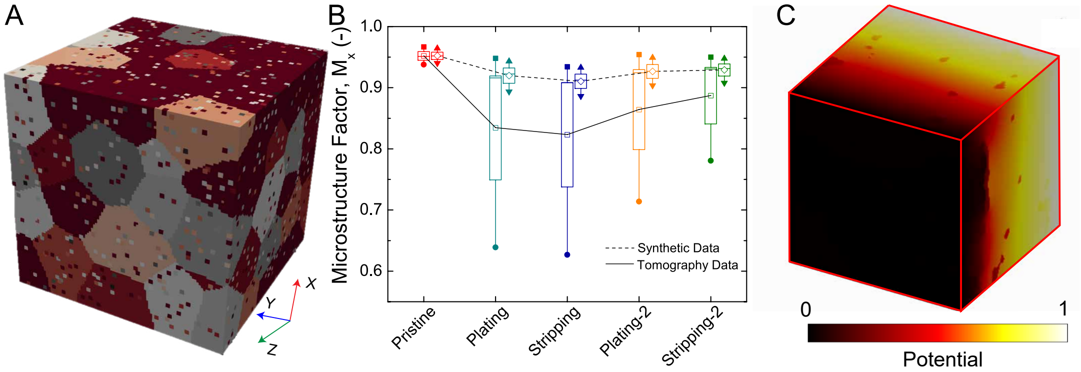

Figure 5: (a) A typical physical domain used for meso-scale simulations. Polycrystalline materials with grain, grain boundary, and pore segregation are evaluated. Domain sizes of 100x100x100 μm^3 are used for the simulation. (b) Microstructure factor (ratio of local property/bulk property) estimated along the X-direction (along Li|SE|Li) of the domain from the tomography and synthetic data set. Tomography dataset uses the binarized reconstruction images as input for the simulations, while synthetic dataset uses isotropic domains generated from the quantified physical parameters (c) Visualization of polarization gradient through the domain under constant potential difference.

To further ascertain the influence of the spatial heterogeneity, mesoscale modelling was carried out for representative simulation domains from interfacial region of LLZO electrolyte. Two data-set formulations were used: a) tomography data which employed the imaged domain directly and b) synthetic data which employed isotropic domains generated from physical parameters (porosity, pore size and grain size) identified from the experimental results. Mesoscale modeling enables explicit definitions of grains, pores as well as grain boundaries to ascertain effective bulk properties of materials (Fig 5a). Microstructure Factor (M$_x$, M$_y$ and M$_z$) is defined as the ratio of the local conductivity/Youngs' modulus estimated along the X-, Y- and Z- direction in the simulated domain to the theoretical value for LLZO. Mean, maximum and minimum microstructure factors have been calculated during electrochemical cycling for both the synthetic and experimental datasets. A strong impact of sample microstructure anisotropy is seen in the tomography data-set with X- direction showing markedly higher variation across different electrochemical steps in microstructure factor compared to Y- and Z- directions (Fig. 5b, S10). In contrast, the synthetic data (isotropic domains) show only a small variation linked to the changes in the effective microstructure. Additionally, the tomography domains show a higher spread (minimum, maximum) compared to the isotropic domains signifying a large heterogenity in local transport and mechanical properties. Identical behavior is seen for the for multiple Li|LLZO systems studied, with comparatively lower anisotropy related fluctuations (variations along X-, Y- and Z- direction). These results clearly show that macroscopic properties of conductivity and Youngs modulus are affected by microstructural heterogeneity. Higher plating density is anticipated in regions around the domains showing lower transport properties to ensure mass balance across the interface. High plating density around these regions leads to stress accumulation which can subsequently lead to cracking/filament propagation through the electrolyte at the regions with the lower effective properties.

Careful experimental design enables high resolution X-ray imaging of lithium metal. High contrast reconstructions and advanced machine learning methods enable segmentation of lithium and pores in *in situ* conditions. This data provides physical insight into microstructure transformation in lithium metal and the solid electrolyte upon cycling. Hotspots in lithium metal electrodes are correlated with the presence of anisotropic microstructures within the solid electrolyte. Mesoscale and pore network modeling results conclusively show local variations in effective properties of the electrolyte at the electrode interface. Local domains showing lower effective properties are construed to be regions where failure modes are initiated due to stress and flux distributions around these regions. Lithium metal electrode kinetics at solid electrolyte interfaces are distinct from liquid electrolytes. The imaging resolution and contrast described here lays the ground work for future studies on lithium electrode kinetics.

Supporting Information Available

Experimental Methods, additional figures for statistics.

Acknowledgement

The authors were supported by the National Science Foundation under grant No. 1847029. The authors acknowledge the Vanderbilt Institute of Nanoscience and Engineering (VINSE) for access to their shared characterization facilities. This research used resources of the Advanced Photon Source, a U.S. Department of Energy (DOE) Office of Science User Facility operated for the DOE Office of Science by Argonne National Laboratory under Contract No. DE-AC02-06CH11357.

References

(1) Hatzell, K. B.; Chen, X. C.; Cobb, C.; Dasgupta, N. P.; Dixit, M. B.; Marbella, L. E.; McDowell, M. T.; Mukherjee, P.; Verma, A.; Viswanathan, V.; Westover, A.; Zeier, W. G. Challenges in lithium metal anodes for solid state batteries. *ACS Energy Letters* **2020**, *5*, 922–934.

(2) Randau, S.; Weber, D. A.; Kötz, O.; Koerver, R.; Braun, P.; Weber, A.; Ivers-tiffée, E.; Adermann, T.; Kulisch, J.; Zeier, W. G.; Richter, F. H.; Janek, J. Benchmarking the performance of all-solid-state lithium batteries. *Nature Energy* **2020**, Advance Article.

(3) Monroe, C.; Newman, J. Dendrite Growth in Lithium/Polymer Systems A Propagation Model for Liquid Electrolytes Under Galvanostatic Conditions. *Journal of The Electrochemical Society* **2003**, *150*, A1377–A1384.

(4) Shen, F.; Dixit, M.; Xiao, X.; Hatzell, K. The Effect of Pore Connectivity on Li Dendrite

Propagation Within LLZO Electrolytes Observed with Synchrotron X-ray Tomography. *ACS Energy Letters* **2018**, acsenergylett.8b00249.

(5) Kasemchainan, J.; Zekoll, S.; Spencer Jolly, D.; Ning, Z.; Hartley, G. O.; Marrow, T. J.; Bruce, P. G. Critical stripping current leads to dendrite formation on plating in 3 lithium anode solid electrolyte cells. *Nature Materials* **2019**,

(6) Wang, M. J.; Choudhury, R.; Sakamoto, J. Characterizing the Li-Solid-Electrolyte Interface Dynamics as a Function of Stack Pressure and Current Density. *Joule* **2019**, 1–14.

(7) Fan, X.; Ji, X.; Han, F.; Yue, J.; Chen, J.; Chen, L.; Deng, T.; Jiang, J.; Wang, C. Fluorinated solid electrolyte interphase enables highly reversible solid-state Li metal battery. *Science Advances* **2018**, *4*, 1–11.

(8) Bay, M. C.; Wang, M.; Grissa, R.; Heinz, M. V.; Sakamoto, J.; Battaglia, C. Sodium Plating from Na-β-Alumina Ceramics at Room Temperature, Paving the Way for Fast-Charging All-Solid-State Batteries. *Advanced Energy Materials* **2020**, *10*, 1–8.

(9) Kazyak, E.; Garcia-Mendez, R.; LePage, W. S.; Sharafi, A.; Davis, A. L.; Sanchez, A. J.; Chen, K. H.; Haslam, C.; Sakamoto, J.; Dasgupta, N. P. Li Penetration in Ceramic Solid Electrolytes: Operando Microscopy Analysis of Morphology, Propagation, and Reversibility. *Matter* **2020**, *2*, 1025–1048.

(10) Wang, M.; Wolfenstine, J. B.; Sakamoto, J. Electrochimica Acta Temperature dependent fl ux balance of the Li / Li 7 La 3 Zr 2 O 12 interface. **2019**, *296*, 842–847.

(11) Sharafi, A.; Haslam, C. G.; Kerns, R. D.; Wolfenstine, J.; Sakamoto, J. Controlling and Correlating the Effect of Grain Size with the Mechanical and Electrochemical Properties of Li7La3Zr2O12 Solid-State Electrolyte. *Journal of Materials Chemistry A* **2017**, *5*, 21491–21504.

(12) Barai, P.; Higa, K.; Srinivasan, V. Lithium dendrite growth mechanisms in polymer electrolytes and prevention strategies. *Physical Chemistry Chemical Physics* **2017**, *19*, 20493–20505.

(13) Mistry, A.; Mukherjee, P. P. Molar Volume Mismatch: a Malefactor for Irregular Metallic Electrodeposition with Solid Electrolytes. *Journal of The Electrochemical Society* **2020**, In Press.

(14) Kasemchainan, J.; Peter, G. All-Solid-State Batteries and their Remaining Challenges. *Johnson Matthey Technology Review* **2018**, *2*, 177–180.

(15) Cheng, L.; Chen, W.; Kunz, M.; Persson, K.; Tamura, N.; Chen, G.; Doe, M. Effect of Surface Microstructure on Electrochemical Performance of Garnet Solid Electrolytes. **2015**,

(16) Xu, X.; Liu, Y.; Wang, J.; Isheim, D.; Dravid, V. P.; Phatak, C.; Haile, S. M. Variability and origins of grain boundary electric potential detected by electron holography and atom-probe tomography. *Nature Materials* **2020**,

(17) Zhang, X.; Wang, Q. J.; Harrison, K. L.; Roberts, S. A.; Harris, S. J. Pressure-Driven Interface Evolution in Solid-State Lithium Metal Batteries. *Cell Reports Physical Science* **2020**, *1*, 100012.

(18) Han, F.; Westover, A. S.; Yue, J.; Fan, X.; Wang, F.; Chi, M.; Leonard, D. N.; Dudney, N. J.; Wang, H.; Wang, C. High electronic conductivity as the origin of lithium dendrite formation within solid electrolytes. *Nature Energy* **2019**, *4*, 187–196.

(19) Porz, L.; Swamy, T.; Sheldon, B. W.; Rettenwander, D.; Frömling, T.; Thaman, H. L.; Berendts, S.; Uecker, R.; Carter, W. C.; Chiang, Y. Mechanism of Lithium Metal Penetration Through Inorganic Solid Electrolytes. *Advanced Energy Materials* **2017**, *7*, 1701003.

(20) Yu, S.; Siegel, D. J. Grain Boundary Softening: A Potential Mechanism for Lithium Metal Penetration through Stiff Solid Electrolytes. *ACS Applied Materials & Interfaces* **2018**, *10*, 38151–38158.

(21) Barroso-Luque, L.; Tu, Q.; Ceder, G. An Analysis of Solid-State Electrodeposition-Induced Metal Plastic Flow and Predictions of Stress States in Solid Ionic Conductor Defects. *Journal of The Electrochemical Society* **2020**, *167*, 020534.

(22) Aguesse, F.; Manalastas, W.; Buannic, L.; Lopez del Amo, J. M.; Singh, G.; Llordés, A.; Kilner, J. Investigating the Dendritic Growth during Full Cell Cycling of Garnet Electrolyte in Direct Contact with Li Metal. *ACS Apllied Materials & Interfaces* **2017**, *9*, 3808–3816.

(23) Lewis, J. A.; Javier, F.; Cortes, Q.; Boebinger, M. G.; Tippens, J.; Marchese, T. S.; Kondekar, N.; Liu, X.; Chi, M.; Mcdowell, M. T. Interphase Morphology between a Solid-State Electrolyte and Lithium Controls Cell Failure. *ACS Energy Letters* **2019**, *4*, 591–599.

(24) Ma, C.; Cheng, Y.; Yin, K.; Luo, J.; Shara, A.; Sakamoto, J.; Li, J. Interfacial Stability of Li Metal Solid Electrolyte Elucidated via in Situ Electron Microscopy. **2016**,

(25) Maslyn, J. A.; Frenck, L.; Loo, W. S.; Parkinson, D. Y.; Balsara, N. P. Extended cycling through rigid block copolymer electrolytes enabled by reducing impurities in lithium metal electrodes. *ACS Applied Energy Materials* **2019**, *2*, 8197–8206.

(26) Maslyn, J. A.; Loo, W. S.; McEntush, K. D.; Oh, H. J.; Harry, K. J.; Parkinson, D. Y.; Balsara, N. P. Growth of Lithium Dendrites and Globules through a Solid Block Copolymer Electrolyte as a Function of Current Density. *The Journal of Physical Chemistry C* **2018**, *122*, acs.jpcc.8b06355.

(27) Harry, K. J.; Hallinan, D. T.; Parkinson, D. Y.; MacDowell, A. A.; Balsara, N. P.

Detection of subsurface structures underneath dendrites formed on cycled lithium metal electrodes. *Nature Materials* **2014**, *13*, 69–73.

(28) Fu, C.; Venturi, V.; Kim, J.; Ahmad, Z.; Ells, A. W.; Viswanathan, V.; Helms, B. A. Universal chemomechanical design rules for solid-ion conductors to prevent dendrite formation in lithium metal batteries. *Nature Materials* **2020**,

(29) Shui, J. L.; Okasinski, J. S.; Kenesei, P.; Dobbs, H. A.; Zhao, D.; Almer, J. D.; Liu, D. J. Reversibility of anodic lithium in rechargeable lithium-oxygen batteries. *Nature Communications* **2013**, *4*.

(30) Endrizzi, M. X-ray phase-contrast imaging. *Nuclear Instruments and Methods in Physics Research, Section A: Accelerators, Spectrometers, Detectors and Associated Equipment* **2018**, *878*, 88–98.

(31) Dowd, B. A.; Campbell, G. H.; Marr, R. B.; Nagarkar, V. V.; Tipnis, S. V.; Axe, L.; Siddons, D. P. Developments in synchrotron x-ray computed microtomography at the National Synchrotron Light Source. Proc. SPIE 3772, Developments in X-Ray Tomography II. 1999; pp 224–236.

(32) Zhang, Y.; Yu, H. Convolutional Neural Network Based Metal Artifact Reduction in X-Ray Computed Tomography. *IEEE Transactions on Medical Imaging* **2018**, *37*, 1370–1381.

(33) Dung, C. V.; Anh, L. D. Autonomous concrete crack detection using deep fully convolutional neural network. *Automation in Construction* **2019**, *99*, 52–58.

(34) Guo, Y.; Liu, Y.; Georgiou, T.; Lew, M. S. A review of semantic segmentation using deep neural networks. *International Journal of Multimedia Information Retrieval* **2018**, *7*, 87–93.

(35) Wang, H.; Wang, Y.; Zhang, Q.; Xiang, S.; Pan, C. Gated convolutional neural network for semantic segmentation in high-resolution images. *Remote Sensing* **2017**, *9*, 1–15.

(36) Frenck, L.; Sethi, G. K.; Maslyn, J. A.; Balsara, N. P. Factors That Control the Formation of Dendrites and Other Morphologies on Lithium Metal Anodes. *Frontiers in Energy Research* **2019**, *7*.

(37) Yakubovskiy, P. Segmentation Models. `https://github.com/qubvel/segmentation_models`, 2019.

(38) Tjaden, B.; Brett, D. J.; Shearing, P. R. Tortuosity in electrochemical devices: a review of calculation approaches. *International Materials Reviews* **2018**, *63*, 47–67.

(39) Dixit, M. B.; Regala, M.; Shen, F.; Xiao, X.; Hatzell, K. B. Tortuosity Effects in Garnet-Type Li$_7$La$_3$Zr$_2$O$_{12}$ Solid Electrolytes. *ACS Applied Materials & Interfaces* **2018**, *11*, 2022–2030.

Graphical TOC Entry